AIP | Journal of Applied Physics

Synergistic etch rates during low-energetic plasma etching of hydrogenated amorphous carbon

T. A. R. Hansen, J. W. Weber, P. G. J. Colsters, D. M. H. G. Mestrom, M. C. M. van de Sanden et al.

Citation: J. Appl. Phys. 112, 013302 (2012); doi: 10.1063/1.4730924
View online: http://dx.doi.org/10.1063/1.4730924
View Table of Contents: http://jap.aip.org/resource/1/JAPIAU/v112/i1
Published by the American Institute of Physics.

Related Articles

Transparent superhydrophobic/superhydrophilic coatings for self-cleaning and anti-fogging
Appl. Phys. Lett. 101, 033701 (2012)

Enhanced electrical and dielectric properties of polymer covered silicon nanowire arrays
Appl. Phys. Lett. 101, 023114 (2012)

Application of hydrogenation to low-temperature cleaning of the Si(001) surface in the processes of molecular-beam epitaxy: Investigation by scanning tunneling microscopy, reflected high-energy electron diffraction, and high resolution transmission electron microscopy
J. Appl. Phys. 112, 014311 (2012)

Extremely high extinction ratio terahertz broadband polarizer using bilayer subwavelength metal wire-grid structure
Appl. Phys. Lett. 101, 011101 (2012)

Energy distribution and quantum yield for photoemission from air-contaminated gold surfaces under ultraviolet illumination close to the threshold
J. Appl. Phys. 111, 124914 (2012)

Additional information on J. Appl. Phys.

Journal Homepage: http://jap.aip.org/
Journal Information: http://jap.aip.org/about/about_the_journal
Top downloads: http://jap.aip.org/features/most_downloaded
Information for Authors: http://jap.aip.org/authors

ADVERTISEMENT

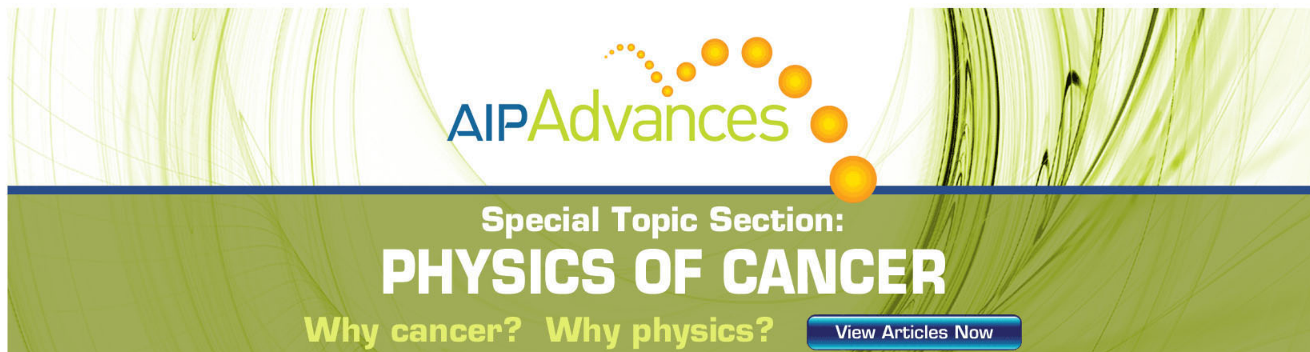

Downloaded 22 Jul 2012 to 130.209.6.40. Redistribution subject to AIP license or copyright; see http://jap.aip.org/about/rights_and_permissions

Synergistic etch rates during low-energetic plasma etching of hydrogenated amorphous carbon

T. A. R. Hansen,[a] J. W. Weber, P. G. J. Colsters, D. M. H. G. Mestrom,
M. C. M. van de Sanden, and R. Engeln[b]
Department of Applied Physics, Eindhoven University of Technology, P.O. Box 513, 5600 MB Eindhoven, The Netherlands

(Received 7 March 2012; accepted 26 May 2012; published online 5 July 2012)

The etch mechanisms of hydrogenated amorphous carbon thin films in low-energetic (<2 eV) high flux plasmas are investigated with spectroscopic ellipsometry. The results indicate a synergistic effect for the etch rate between argon ions and atomic hydrogen, even at these extremely low kinetic energies. Ion-assisted chemical sputtering is the primary etch mechanism in both Ar/H_2 and pure H_2 plasmas, although a contribution of swift chemical sputtering to the total etch rate is not excluded. Furthermore, ions determine to a large extent the surface morphology during plasma etching. A high influx of ions enhances the etch rate and limits the surface roughness, whereas a low ion flux promotes graphitization and leads to a large surface roughness (up to 60 nm). © *2012 American Institute of Physics*. [http://dx.doi.org/10.1063/1.4730924]

I. INTRODUCTION

Carbon is widely used as wall material inside existing experimental nuclear fusion reactors. The next generation fusion reactor ITER will likewise use carbon in part of the divertor. Significant erosion of ITER's divertor wall is expected due to the steady state particle and energy flux of up to $10^{24}\,m^{-2}\,s^{-1}$ and up to $10\,MW\,m^{-2}$, respectively.[1–3] This eroded carbon material is then redeposited throughout the reactor in the form of hydrogenated amorphous carbon (*a*-C:H). Such deposits have been found within the divertor, thus close to the carbon source, but also elsewhere inside existing fusion reactors.[4,5] However, the presence of these *a*-C:H layers is not without concern. The primary concern is co-deposition of tritium, a radioactive hydrogen isotope, and part of the fuel mixture. This forms a safety issue as well as a fuel inventory problem.[5] ITER will therefore only use a carbon-based divertor wall during the hydrogen and deuterium startup and conditioning phase of the reactor.[6,7] A second issue is performance degradation of the plasma-facing optical components when coated with *a*-C:H.[8,9] *In situ* low-temperature plasma etching will be part of the maintenance procedure of these components since replacement will not always be immediately possible.[8,9] A third issue is that *a*-C:H lacks the good thermo-nuclear properties of the original carbon wall. How these layers and the wall in general behave under the plasma conditions expected in ITER remains an open question.[3] In particular, plasma etching of carbon with an ion energy in between thermal energy and 10 eV has not yet been fully investigated.[10]

Previous studies of carbon etching — with ion energies between 10 eV and 5 keV — have established several etch mechanisms in literature.[11–18] Two of those mechanisms, i.e. chemical sputtering and ion-assisted chemical erosion, describe a synergistic effect in the etch rate when simultaneously exposing *a*-C:H to both radicals and ions (see also Sec. II).[13,17,19] The ion energy is thereby higher than the binding energy ($\sim 3-5$ eV) for the carbon bonds, yet lower than the threshold for physical sputtering ($\sim 32-58$ eV). The difference between both mechanisms lies in the role of the incident ions. These ions either facilitate the thermal desorption of etch products or participate in the etch process by breaking carbon bonds. This paper investigates whether such a synergistic effect also exists for *a*-C:H thin films exposed to a low-temperature plasma with an ion energy below 2 eV. To that end, experiments have been carried out in a linear plasma reactor with pure argon and hydrogen plasmas as well as mixtures thereof. *a*-C:H thin films deposited with plasma-enhanced chemical vapour deposition (PE-CVD) are used as a model material.[20–22] The incident ion flux is thereby determined via electrical probe measurements, while radical fluxes are estimated from previous work in our group. Variations in the particle flux between the different plasma systems can then be accounted for when comparing the etch rates of each system.

The etch rates themselves can be determined with a variety of methods such as colorimetry, contact profilometry, and ellipsometry.[15,17,23–25] In contrast with contact profilometry on graphite, for instance (spectroscopic) ellipsometry (SE) can be applied *in situ* on an *a*-C:H thin film.[15,17,24] Single wavelength ellipsometry is widely used in literature to investigate plasma etching.[15,17,24] Although this method has a high time resolution, the data analysis does not provide a unique solution for the thickness evolution without additional information about the initial thickness. This issue can be circumvented through the use of spectroscopic ellipsometry.[26] Therefore, this paper employs spectroscopic ellipsometry in combination with a B-spline model (Sec. III B) to determine etch rates. The existence of a synergistic effect in

[a] Present address: Imec, Kapeldreef 75, 3001 Leuven, Belgium.
[b] Author to whom correspondence should be addressed. Electronic mail: R.Engeln@tue.nl.

 © 2012 American Institute of Physics

Downloaded 22 Jul 2012 to 130.209.6.40. Redistribution subject to AIP license or copyright; see http://jap.aip.org/about/rights_and_permissions

a plasma with very low ion energy will then be ascertained from a comparison of these etch rates. Not only the etch rates, but also the evolution in surface roughness will be discussed for the different plasma systems. One of the more striking results is the extreme roughening of *a*-C:H in a pure hydrogen plasma. This phenomena will be explained via modification of the surface material by low kinetic energy ions.

II. AMORPHOUS CARBON ETCH MECHANISMS

The different etch mechanisms, as mentioned in the introduction, include chemical erosion, ion-assisted chemical erosion, chemical sputtering, and swift chemical sputtering (SCS). These four etch mechanisms will now be discussed in more detail. The reader is also referred to the review work by Jacob.[33,34]

Chemical erosion can occur when an *a*-C:H sample is exposed to an atomic hydrogen beam.[35–37] An important step in chemical erosion is the conversion of sp^2 into sp^3 groups through *hydrogenation*. This will lead in some situations to the formation of a dangling bond (DB). Passivation of such a DB by another incident hydrogen atom results in the formation of a sp^3 group. The DB can alternatively be passivated through the release of volatile CH_3 (or more general C_xH_y) radical groups, which results in a sp^2 group. A similar (back) conversion of sp^3 into sp^2 groups occurs though *hydrogen abstraction*, with a corresponding release mechanism of volatile hydrocarbon groups. The cross section for hydrogen abstraction is, however, one order of magnitude smaller than hydrogenation.[36] The result of chemical erosion is thus a net increase in sp^3 groups and removal of surface material. The etch rate for sp^2 rich films will also be lower than for sp^2 poor films, when the film is exposed to a constant flux of radicals.[27] Hydrogen abstraction furthermore is an Eley-Rideal process, in which the reaction proceeds directly without the surface first absorbing and thermalizing the incident H atom.[36,38,39]

The erosion yield for chemical erosion with H—which is thermally activated—is negligible below 34 meV (400 K) and varies from 0.001 to 0.1 above 34 meV, with a maximum at 52 meV (600 K).[16,18,35,36,40] These yields were reported for an atomic H flux of $10^{15}-10^{20}\,m^{-2}\,s^{-1}$. H_2 recombination above 600 K causes the reduction in the yield.[1] The activation energy (E_a) for the erosion of a methyl (CH_3) group from the carbon network of an *a*-C:H film falls in the range of $1.6-2.5$ eV (Fig. 1).[27,33,35,36,41] Similar values of $1.7-1.9$ eV are found for graphite etching.[1,42,43] Even though this falls below the binding energy of 3.5 eV of a $C_{network}$-CH_3 bond, the energy gain from re-hybridization of the carbon network from sp^3 to sp^2 accounts for the low activation energy.[33,36,44] Weakly bonded hydrocarbons—either created after a chemical erosion reaction or (re-)deposited on the *a*-C:H surface—have an E_a on the order of 0.6 eV for thermal desorption.[45,46] Breaking the $C_{network}$–CH_3 bond is thus the rate-limiting step in chemical erosion.[35]

The erosion can moreover be enhanced by simultaneously irradiating the surface with ions ($10^{16}-10^{24}$ m^{-2} s^{-1}).[1,10,13,14,16–18,40,47,48] The kinetic energy of the incident ions is thereby below the threshold for physical sputtering

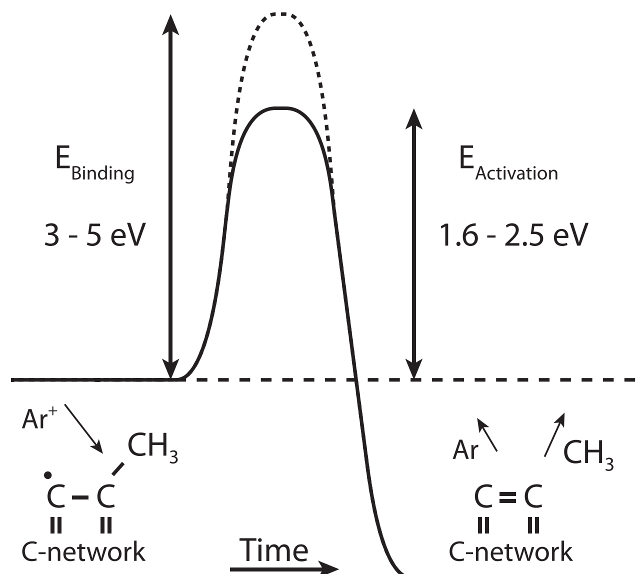

FIG. 1. The release of a methyl group from the carbon network, i.e., *a*-C:H, is thermally activated. Moreover, energy gains from relaxation of the carbon network give rise to a low activation energy with respect to the binding energy. In ion-assisted chemical erosion, this activation energy can be provided for by an ion hitting the surface.

(32 eV for H^+; 58 eV for Ar^+).[13] When the ions transfer sufficient kinetic energy for the erosion of a CH_3 (or higher C_xH_y) radical group, but do not break any bonds themselves, the process is called ion-assisted chemical erosion.[13] Chemical sputtering is a similar process, in which the incident ions do break carbon bonds within their surface penetration depth.[17–19,49,50] The incident hydrogen radicals immediately passivate the newly formed DBs, thereby creating hydrocarbon groups that will eventually desorb. The energy required to break C-C and C-H bonds is about $3-5$ eV, with the energy of the incident ion at least a few eV's above that.[51] The erosion yield ($10^{-3}-10^{1}$) depends furthermore on the ion energy and incident ion flux and, all else being equal, is higher for *a*-C:H than for graphite.[1,10,14,16,18,40,45,47,48]

The fourth and last mechanism explained here is swift chemical sputtering, which first came to light via numerical modelling of very high hydrogen fluxes (up to 10^{29} m^{-2} s^{-1}) incident on an *a*-C:H surface.[52–55] An incident hydrogen radical enters the space occupied by a carbon-carbon bond. The nuclei are no longer shielded from each other and the bond will break, resulting in a dangling bond and a newly formed CH bond. This will remove material from the surface if the carbon bond was only the remaining connection to the carbon network of the *a*-C:H sample. Passivation of the DB occurs again either by another incident hydrogen atom or through the release of a CH_3 radical group, provided that the DB became part of the carbon network. As the name already suggests, SCS is a very fast process that leaves no opportunity to the carbon network to thermalize before the bond is broken. SCS has no inherent temperature-dependent etch rate, although numerical simulations reveal a threshold of $\sim 1-3$ eV.[52,55,56] The SCS yield for kinetic energies below 10 eV varies from 0.003 to 0.009 between 300 and 700 K.[52,54] In this description, the incident hydrogen bonds

Downloaded 22 Jul 2012 to 130.209.6.40. Redistribution subject to AIP license or copyright; see http://jap.aip.org/about/rights_and_permissions

to the eroded material. Salonen *et al.*, however, note that the hydrogen radical would also sometimes bond to the surface itself.[52]

Two etch mechanisms which fall far outside of the experimental conditions of this paper are radiation enhanced sublimation (>1300 K substrate temperature) and hydrogen enhanced physical sputtering (150 eV argon ions). Another differentiator besides the ion energy is that the radical flux far exceeds the ion flux in both ion-assisted chemical erosion and chemical sputtering, whereas this situation is reversed in hydrogen enhanced physical sputtering (see, e.g. Refs. 57 and 58 for more details).

III. HYDROGENATED AMORPHOUS CARBON

The properties of hydrogenated amorphous carbon are to a large extent determined by the sp^2 to sp^3 ratio and hydrogen content of the material.[59,60] The variety in sp^2 to sp^3 ratio and hydrogen content leads to several different types of *a*-C:H, many of which can be deposited by PE-CVD.[20–22,59] PE-CVD is a well known technique in our group and is used in this work as well to prepare *a*-C:H samples for etching. The deposited carbon material should furthermore be seen as a generic material model for carbon rather than the study of a very specific type of *a*-C:H. Even so, the (initial) properties of these samples together with the deposition process are described in Sec. III A. *In situ* spectroscopic ellipsometry (Sec. III B) monitors sample properties such as thickness and roughness during plasma etching.

A. Deposition and characteristics

a-C:H samples are pre-deposited by plasma enhanced chemical vapour deposition on a similar reactor as described in Sec. IV.[20–22] To deposit these samples, acetylene (15 sccs) is added via an injection ring to an Ar plasma (100 sccs, 75 A, 4.5 kW) at a background (BG) pressure of 30 Pa. The substrate temperature is 250 °C, with a backflow of helium (1 sccs) for improved thermal contact. Last, a deposition time of 30 s results in a film thickness of about 1 μm. The film carrier is a Si wafer with a 1.6 nm native oxide layer.

After deposition, these samples are stored in a desiccator to minimize exposure to the ambient air.[61] Of every deposited sample, a surface area of 200 mm^2 is exposed to the plasma during the etching experiments discussed in this paper. Previous studies have characterized these *a*-C:H samples as graphitic carbon (i.e., a high sp^2 content) with less than 5% of sp^1 bonds.[21,62] The sp^2 to sp^3 ratio is estimated to be around 0.52.[63] With a density of 1.7×10^6 g/m^3, an atomic content of 30% hydrogen and 70% carbon, the total number of atoms # in a 1 μm thick film is estimated to be 7×10^{19}. For a given etch rate ER in nm/min (Sec. III B) and the total ion and radical flux Γ in $m^{-2}\,s^{-1}$, the yield Y of eroded carbon atoms per incident particle can then be calculated with $Y = 9.95 \times 10^{17} \times ER/\Gamma$.

B. *In situ* spectroscopic ellipsometry

In situ measurements are performed with a rotating compensator ellipsometer measuring in the visible and near infrared wavelength range (0.75 – 5.0 eV, J. A. Woollam Co., Inc. M2000U). The analysis software is CompleteEASE 3.55 and 4.06, from J. A. Woollam Co., Inc. The ellipsometer is mounted under an angle of $\sim 68^\circ$. The data acquisition rate of the ellipsometer is typically set to 25 revolutions of the compensator per measurement (r/m) for the plasma mixtures and 100 r/m for the pure plasmas, with the high accuracy mode enabled. This indicates that each datapoint is averaged over 25 or 100 scans.

Analysis of spectroscopic ellipsometry data requires a (multi-layered) model that describes the interaction of the incident light with — as in our case — a diamond-like carbon thin film. The dielectric function of *a*-C:H is commonly described by one or more Tauc-Lorentz oscillators.[26,31] However, as demonstrated in a previous paper on the film growth of these *a*-C:H samples, the use of a purely mathematical description of the dielectric function by means of basis-splines (B-splines) is also possible.[22,32] This so-called *B-spline model* yields the thickness (d_{bulk}), roughness ($d_{roughness}$), and the dielectric function of the *a*-C:H sample.[22] The void fraction of the roughness layer, which is modeled by a Bruggeman's effective medium approximation (EMA),[64] can be included in the fit parameters as well. Even so, fitting both the void fraction of the roughness layer and the dielectric function of the bulk layer causes correlation in the fitting parameters. To avoid this, the void fraction is always fixed at 50% when the substrate temperature changes during plasma exposure.

The B-spline model does not include a thin top layer with its own dielectric function and thickness, even though both hydrogen ions and radicals — when present in the plasma — are known to modify the first few nanometers of the carbon layer in terms of the sp^2 to sp^3 ratio.[27,30] However, these changes were reported for very high ion energies (90 – 800 eV),[27–29] whereas the ion energy in an expanding thermal plasma at floating potential is less than a few eV's (see also Sec. IV A). Even though surface material is removed during plasma etching at the expense of this top layer, the underlying bulk material is continuously converted. Or viewed differently, the top layer maintains a semi-constant thickness while the bulk thickness decreases. Moreover, the thickness of such a top layer would be either (much) smaller or comparable in size to the roughness layer of our samples. In addition, because our samples are homogeneous after deposition,[22] the dielectric function of this top layer cannot be determined beforehand since it has an effective thickness of zero at the onset of plasma treatment. The inclusion of a top layer in the model would therefore not yield the preferred results for our purposes. Although there is an apparent contradiction between this modification and excluding a top layer from the model *ab initio*, the etch rate under our plasma conditions can only be susceptible to the sp^2 to sp^3 ratio at the exposed surface.

Both growth rates and etch rates of a carbon sample are given by the first order derivative of the total thickness (i.e., $d_{total} = d_{bulk} + (1 - f_{void}) \times d_{roughness}$) as a function of time. The etch rates discussed in this paper have also been smoothed by a first order Savitzky-Golay filter, with a window of 10 points wide. Unless otherwise specified, *etch rate* in this text refers to the overall etch rate for the entire film.

Downloaded 22 Jul 2012 to 130.209.6.40. Redistribution subject to AIP license or copyright; see http://jap.aip.org/about/rights_and_permissions

Furthermore, the etch rate is proportional to the reaction rate at the surface, provided that the incident particle flux at the surface remains constant. This is the case in these experiments as the plasma conditions are not changed during the entire erosion process of a particular *a*-C:H sample. Last, the Arrhenius equation applies to the reaction rate when the erosion is thermally activated.[15,27,65,66] The activation energy in the Arrhenius equation is determined from a linear fit of the logarithmic etch rate as function of the inverse temperature.

IV. EXPERIMENTAL SETUP

The experimental setup in which the hydrogenated amorphous carbon samples are exposed to a plasma is described in Sec. IV A. A capacitive probe, described in Sec. IV B, is used to measure the ion flux at the position of the sample.

A. Expanding thermal plasma

The experimental setup is a linear plasma reactor with a cascaded arc as plasma source (Fig. 2). The arc is operated on a 60 A dc current and has an input power of 2.7 – 9 kW, depending on the gas mixture. It operates under high pressure and generates a thermal plasma which expands into a low pressure vacuum chamber with a background pressure set between 20 and 270 Pa. The substrate is located about 32 cm downstream from the arc. At the exit of the arc, the electron temperature $\hat{T}_e$ is about 1 – 1.2 eV. This value drops to less than 0.3 eV (typically about 0.1 eV) at the position of the substrate.[67] When no external bias is applied on the substrate during plasma etching, the peak of the ion energy distribution (IED) at floating potential is situated around 1 – 2 eV as was previously measured by Kudlacek *et al.* under similar plasma conditions.[68] The arc is in this paper operated on Ar, H_2, D_2 or a gas mixture thereof. In previous work in our group, the dominant ion near the substrate was determined for each gas mixture. This is Ar^+ and H_3^+ (D_3^+) for a pure argon and pure hydrogen (deuterium) plasma, respectively.[69–71] The dominant ion in case of an Ar/H_2 (Ar/D_2) plasma depends on the gas mixture. With less than 2%–3% of H_2 (D_2), the ion composition consists of Ar^+, ArH^+ (ArD^+), and H_3^+ (D_3^+).[72–74] In gas mixtures with a higher H_2 content, that role is again fulfilled by H_3^+.[75] The cascaded arc and plasma expansion itself have been characterized in more detail elsewhere, e.g. Refs. 67 and 76).

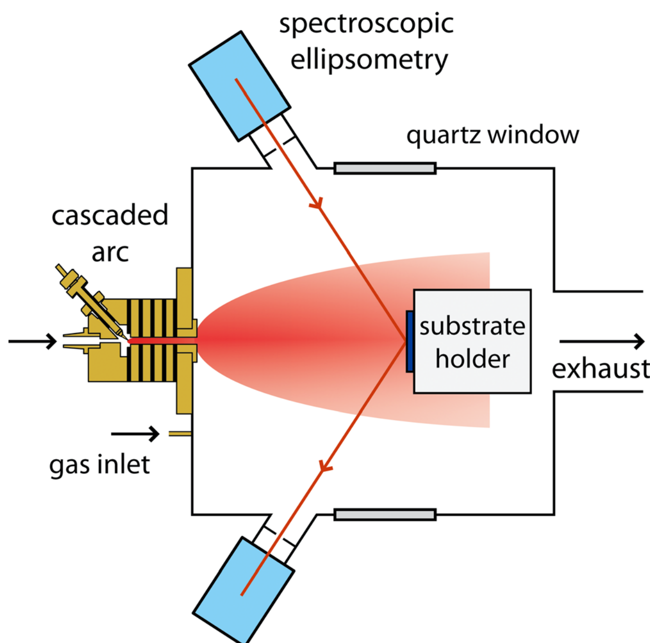

FIG. 2. Schematic cross-section of the reactor.

Before any plasma is generated, the reactor is pumped down to a minimum base pressure of 5×10^{-5} mbar. To minimize water content, the reactor wall is also kept at an elevated temperature of close to 310 K. The reactor is furthermore equipped with a shutter that protects a sample from direct exposure to the expanding thermal plasma. Prior to shutter retraction, a pure argon plasma is burned for 3–5 min to provide additional wall heating for outgassing and to replace, as much as possible, any gaseous impurities by argon. Despite these precautions, the presence of minute traces of hydrogen, oxygen, or water in the system cannot be excluded.

Furthermore, a backflow of helium (1 sccs) improves thermal contact between the substrate holder and the substrate (i.e. sample holder) itself. Despite active temperature control, an argon plasma will still heat up the substrate in this reactor. The temperature is therefore registered by a thermocouple, located a few mm's to the side of the sample.

B. Capacitive probe

A direct measurement of the ion flux is obtained by operating a planar Langmuir probe as a so-called ion probe (i.e. a capacitive probe).[77,78] The design, operating procedure, and characterization of an ion probe is described in detail by Petcu *et al.*[78]

Our planar probe is embedded in a sample holder which provides a measurement directly at the position of the sample. The sample holder itself is electrically floating, whereas the collecting area (200 mm^2) is connected to a single external capacitor (12.7 ± 0.1 nF).

A pulsed slope-shape waveform signal (Fig. 1 in Ref. 78) with a downward slope from −5 to −10 V (20 V peak to peak) is applied on this capacitor by means of a waveform generator (TTI TG4001). When the correct frequency is used, the bias voltage on the collecting area is constant (−14 V) during the downward slope. This also results in a constant ion energy, which can be controlled through varying the applied voltage. Thus, both the flux and energy of the ions remain constant by applying a sloped, rather than a squared waveform.

The contribution of the electron current to the total current during the downward slope of the pulse shaped waveform can be neglected in the data analysis of Sec. V A. However, this approach is only valid if the bias voltage is sufficiently negative. The required bias voltage can be calculated from $V_{bias} = T_e \, ln(A) + V_{plasma}$ with $A = R \times \sqrt{2\pi \; m_e/m_i}$. This expression has been derived from the ratio of the ion and electron fluxes.[79] With a conservative estimate of 0.5 eV for the electron temperature and 0.5 V for the plasma potential at the

Downloaded 22 Jul 2012 to 130.209.6.40. Redistribution subject to AIP license or copyright; see http://jap.aip.org/about/rights_and_permissions

position of the substrate, the voltage limits are −3.49 V for H_3^+ and −4.15 V for Ar^+.

The current in the electric circuit (I_c) is determined from the time variation in the absolute voltage drop ($|V_{drop}|$) over the capacitor during the downward slope (Eq. (1)), which is equal to the ion current (I_{ion}) collected by the probe (Eq. (2)).

$$I_c = C\, d|V_{drop}|/dt, \qquad (1)$$

$$I_{ion} = eA\Gamma_{ion}, \qquad (2)$$

with Γ_{ion} the ion flux, e the elementary charge, and A the collecting area of the probe. Rewriting both equations yields a direct expression for the ion flux, which is independent of the ion mass,

$$\Gamma_{ion} = \frac{C}{eA}\,\frac{d|V_{drop}|}{dt}. \qquad (3)$$

V. EXPERIMENTAL RESULTS

This section on the experimental results is divided into three parts. The first part concerns the ion and radical flux incident on the *a*-C:H sample. The second part deals with the interaction between amorphous carbon and a pure hydrogen plasma, whereas Ar/H_2 and Ar/D_2 plasma mixtures are used in part three.

A newly deposited sample was used for every measurement. The deposition conditions and sample characteristics are mentioned in Sec. III A. Starting values for the thickness, roughness, and dielectric function for the samples discussed in this paper are determined prior to plasma exposure.

A. Incident ion and radical flux

The etch rate of *a*-C:H depends on the incident particle flux. In this section, the ion flux is measured directly at the surface by an ion probe, while estimates for the atomic hydrogen flux are given.

Fig. 3 shows the ion and H-flux in a pure hydrogen plasma (50 sccs H_2) as a function of background pressure.

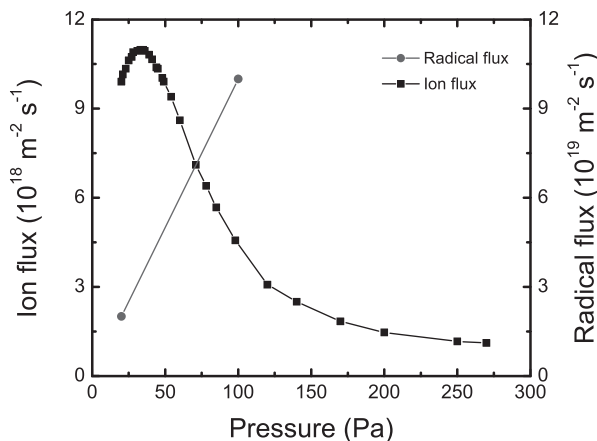

FIG. 3. Ion and radical flux in a pure hydrogen plasma (50 sccs, 60 A). Ion flux measurements are taken with a capacitive probe, at the position of the sample. The highest ion flux can be found at 33 Pa. Radical fluxes are estimated from previous work.[80]

The width of the plasma expansion at low pressures is wider than the collecting area of the ion probe. An increase in background pressure focuses the plasma onto the ion probe, which leads to higher measured fluxes. The plasma chemistry, however, is dominated by charge transfer and dissociative recombination reactions, which increases in number together with the background pressure. This leads to a reduction in the ion flux. The competition between both effects results in a maximum for the ion flux at 33 Pa, as observed in Fig. 3. The measurement error with electrical probes is on the order of 10%–20%.[78]

The atomic hydrogen flux (Γ_H) in Fig. 3 is estimated from the density and thermal velocity of atomic H,[79]

$$\Gamma = \frac{n v_{thermal}}{4} = \frac{n\sqrt{kT/M}}{4}, \qquad (4)$$

with T the thermal temperature (0.1 eV) and M the hydrogen mass (1 amu). Atomic hydrogen densities have been previously measured in our group for similar plasma conditions.[80] The reported density at 20 Pa is $\sim 2 \times 10^{19}$ m^{-3}, which is 5 times lower than the density of $\sim 10^{20}$ m^{-3} at 100 Pa.[80] The H density and thus flux at intermediate pressures are based on a linear extrapolation of these values. Higher background pressures lead to higher radical fluxes, whereas a maximum in the ion flux is observed in the—relatively speaking—low pressure range.

The ion flux has also been measured in pure and mixed argon plasmas for a background pressure of 100 Pa. The ion current in a pure argon plasma (50 sccs Ar) was too high to be measured directly with the ion probe. Ion saturation current measurements under the same plasma conditions, however, could be obtained with a double Langmuir probe in a similar reactor without substrate. This yields an ion flux of 1.4×10^{22} m^{-2} s^{-1}.[81]

The gas flow for the mixed plasma systems consists of 50 sccs Ar and 1 sccs of either H_2 or D_2. H_2 is injected via the arc or directly into the BG, whereas D_2 is only injected via the arc. The ion flux in these three systems as measured with the ion probe can be found in Table I. Immediately apparent is the drastic reduction (2–3 orders of magnitude) in ion flux when H_2 or D_2 is added to the reactor. Only the radical density in an Ar/H_2:BG plasma was previously measured in our group under these plasma conditions. An atomic H density of 2.8×10^{19} m^{-3} yields a flux of 2.2×10^{22} m^{-2} s^{-1}, assuming a thermal temperature of 0.1 eV. This is more than 2 orders of magnitude higher than the ion flux. H and D fluxes for the two remaining systems are expected to have

TABLE I. The ion and radical fluxes for different plasma systems. Arc current and background pressure are 60 A and 100 Pa, respectively, for all systems. BG indicates gas injection directly in the background of the reactor.

Plasma conditions	Ion flux (m^{-2} s^{-1})	Radical flux (m^{-2} s^{-1})
50 sccs Ar	1.4×10^{22}	n/a
50 sccs Ar, 1 sccs H_2 (BG)	1.1×10^{20}	2.3×10^{22}
50 sccs Ar, 1 sccs H_2 (arc)	8.5×10^{19}	
50 sccs Ar, 1 sccs D_2 (arc)	1.7×10^{20}	

Downloaded 22 Jul 2012 to 130.209.6.40. Redistribution subject to AIP license or copyright; see http://jap.aip.org/about/rights_and_permissions

the same order of magnitude. Etch rates for *a*-C:H under these plasma conditions are determined in Sec. V C.

B. Changes in a-C:H properties

The results in this section will show the influence of a pure hydrogen plasma (50 sccs, 60 A) on the characteristics of an *a*-C:H sample as well as the influence of these evolving characteristics on the etch rate.

First, changes in the sample's morphology are determined. The background pressure and substrate temperature are set to a constant 46 Pa and 241 ± 1 °C respectively. The dielectric function is determined beforehand and fixed for every thickness (i.e., every datapoint). The unbiased maximum likelihood estimator χ^2—which is a measure of the fit quality[77,82]—for this particular sample reaches 68. If the void fraction is varied, on the other hand, χ drops below 25 as can be seen in Fig. 4. Also shown are the time evolution in the thickness, the roughness, the etch rate, and the void fraction of the EMA roughness layer during plasma exposure.

During plasma exposure, the roughness increases continuously from 7 to 62 nm. The initial roughness of 7 nm is thereby larger than the as-deposited roughness due to the pretreatment with an argon plasma. A roughening is also seen in the cross-sectional scanning electron microscopy (SEM; model JEOL 7500FA) images (Fig. 5). The first image was taken from an as-deposited sample, whereas the sample in the second image was exposed to a hydrogen plasma. The large surface features are debris as a result from breaking the sample. Also notice the reduction in thickness between those two images. Although a roughness of 60 nm is too large for an AFM to probe,[83] AFM measurements do show a change in topography from bump-like structures to more peaked structures (Fig. 6). The AFM (NT-MDT solver P47 with NSG 10 tips) is operated in tapping mode to avoid damage to the sample and scans a 2 × 2 μm^2 area with a resolution of 512 × 512 points. The RMS roughness of the AFM and SE roughnesses of the as-deposited sample are 4.8 and 7.6 ± 0.1 nm, respectively. These values are 11.8 and 25.0 ± 0.2 nm, respectively, for the etched sample in Fig. 6, which had an initial SE roughness of 6.0 ± 0.3 nm. Furthermore, an exponential fit of the autocorrelation function, i.e., the distance beyond which one peak no longer affects another peak, yields an e-folding length of 82.2 ± 1.8 and 69.2 ± 1.5 nm for the as-deposited and etched sample, respectively. This likewise indicates a roughening of the surface.

This change in morphology and the large increase in $d_{roughness}$ indicates a preferential etching mechanism, whereby the surface *valleys* have a locally higher etch rate than the *hills* of the roughness layer. In contrast with the

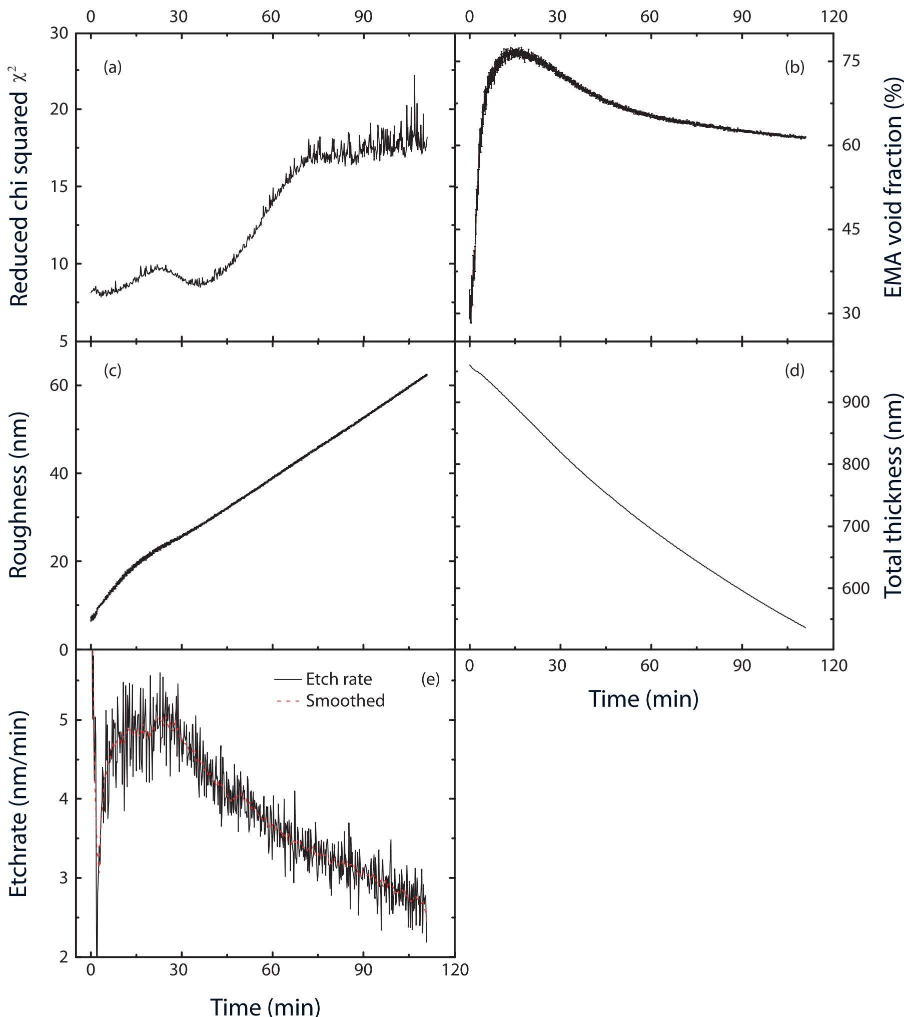

FIG. 4. An a-C:H sample is exposed to a pure hydrogen plasma (50 sccs, 60 A, 46 Pa) at a constant substrate temperature of 241 °C. (a) The fit quality of a B-spline model with variable void fraction, (b) void fraction of the roughness layer, (c) the roughness, (d) thickness, and (e) etch rate of the sample.

Downloaded 22 Jul 2012 to 130.209.6.40. Redistribution subject to AIP license or copyright; see http://jap.aip.org/about/rights_and_permissions

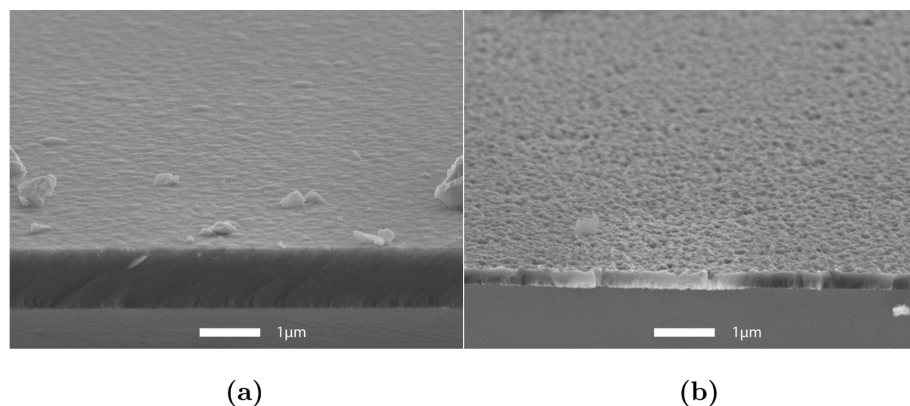

FIG. 5. Cross-sectional SEM images of an a-C:H sample (a) as-deposited and (b) after exposure to a pure hydrogen plasma (50 sccs, 60 A, 100 Pa). An increase in roughness and decrease in thickness can clearly be observed.

roughness, which increases as a function of time, both the void fraction and the etch rate show a maximum as a function of time. The void fraction determined with spectroscopic ellipsometry starts low (31%), but reaches a maximum (77%) rather quickly. Afterwards, it decreases smoothly to 61%. The etch rate exhibits similar behaviour, although the maximum of 5.0 nm/min is reached at a later point in time. The etch rate drops more than 40% in the first 60 min after this maximum, while the reduction in the void fraction is less than 20% for the same length of time. Since the plasma conditions are not changed while etching, the incident ion and radical flux are assumed constant. If the surface area is furthermore assumed to be a linear function of both $d_{roughness}$ and f_{void}, then it can be stated that the etch rate decreases while the total surface area continues to increase.

Second, Fig. 7 shows the temperature dependent etch rate for two different background pressures: 25 Pa and 100 Pa. This confirms that the erosion is thermally activated and that an activation energy can thus be determined from these measurements.[15,27,65,66] The 100 Pa measurement can be described with an E_a of 0.259 ± 0.003 over the inverse temperature range from 1.73×10^{-3} up to 2.54×10^{-3} K^{-1}, as listed in the first part of Table II. A single activation energy will clearly not suffice for the measurement at 25 Pa and is therefore divided into three intervals. The first interval, which goes from 1.81×10^{-3} to 2.54×10^{-3} K^{-1}, is comparable to the measured temperature range at 100 Pa and yields an E_a of 0.284 ± 0.005 eV. The second interval with an E_a of 0.094 ± 0.005 eV continues from 2.54×10^{-3} K^{-1} and extends up to 2.86×10^{-3} K^{-1}. The large drop in etch rate, which is covered by a third interval, has an E_a of 0.094 ± 0.005 eV. The activation energy will be further discussed in Sec. VI A.

Third, the etch rate at 100 Pa in Fig. 7 is 4–9 times higher than the etch rate at 25 Pa. Fig. 3 on the other hand shows that the ion flux at 100 Pa (4.41×10^{18} m^{-2} s^{-1}) is less than half of the ion flux at 25 Pa (1.06×10^{19} m^{-2} s^{-1}), while the atomic H flux increases with a factor of 4 from $\sim 2 \times 10^{22}$ at 25 Pa to $\sim 8 \times 10^{22}$ m^{-2} s^{-1} at 100 Pa. This indicates that the incident atomic H flux plays a dominant role in the erosion process of a-C:H. The yield per total hydrogen flux (i.e. radicals and ions combined) is on the order of 2×10^{-4} at the high temperature range (515 K) and 2×10^{-5} at the low temperature range (350 K), which are lower than the yields found in literature (Sec. II).

The fourth and last point in this section concerns the ion energy itself. Fig. 8 shows the etch rate at 33 Pa, i.e. the highest ion flux according to Fig. 3. The substrate temperature during the measurement increases from about 364 to 371 K. This has a negligible effect on the etch rate as can be seen in Fig. 4. The ion energy is furthermore controlled by means of the capacitive probe (see also Sec. IV B), onto which an a-C:H sample can be clamped. Such a sample acts as an additional capacitor in the electrical circuit, which can distort the applied waveform signal and thus the bias voltage at the sample's surface unless the film thickness d is small relative to the Debye length λ_d,

$$d \ll \varepsilon_r \lambda_d, \tag{5}$$

with ε_r the dielectric constant of the film.[77] A dielectric constant of 5.2 and a Debye length of 30 μm — for an electron density and temperature of 6.1×10^{15} m^{-3} and 0.1 eV, respectively — gives an upper limit of 156 μm for the film thickness.[22] The thickness in the measurement presented here decreases from $\sim$980 to $\sim$870 nm, thus well below this

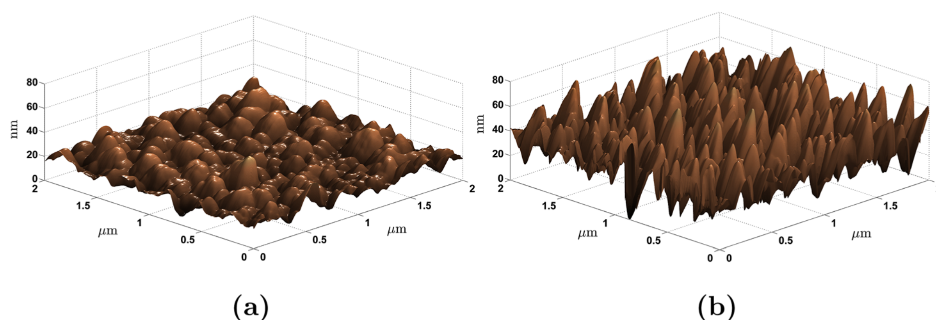

FIG. 6. AFM image of an a-C:H sample (a) as-deposited and (b) after exposure to a pure hydrogen plasma (50 sccs, 60 A, 100 Pa). The plasma exposure has changed the morphology from bump-like features to more peaked features.

Downloaded 22 Jul 2012 to 130.209.6.40. Redistribution subject to AIP license or copyright; see http://jap.aip.org/about/rights_and_permissions

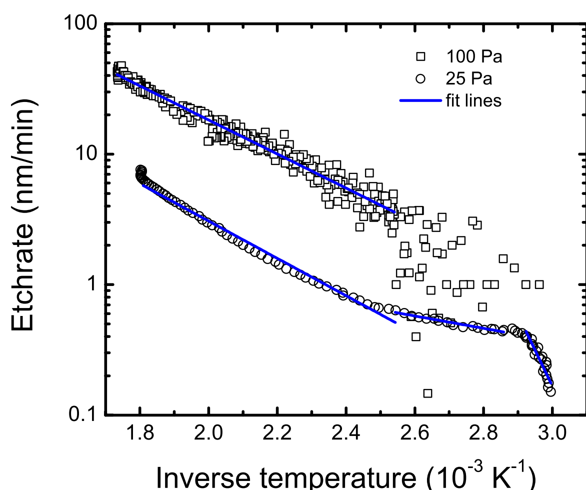

FIG. 7. Etch rate in a pure hydrogen plasma (50 sccs H_2, 60 A). An activation energy is derived from the different fit lines.

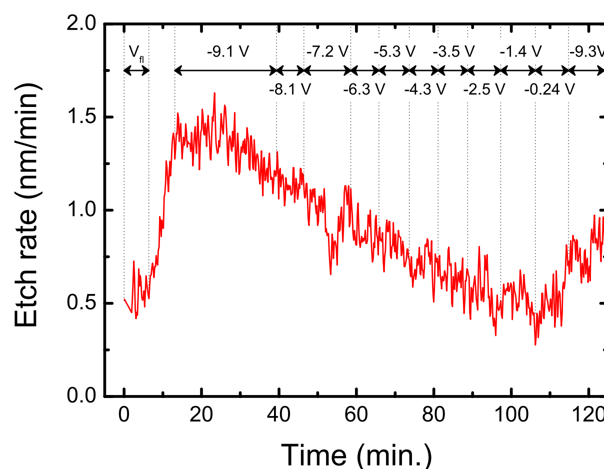

FIG. 8. Etch rate in a pure hydrogen plasma (50 sccs H_2, 60 A, 33 Pa, 91–98 °C $T_{substrate}$) for different ion energies. The bias voltage is indicated in the graph. The smoothing window of the Savitzky-Golay filter is 20 points wide.

upper limit. This thickness evolution furthermore translates into a capacitance of ∼9 to ∼11 nF for the *a*-C:H film. When the 1.6 nm thin native oxide layer of the Si substrate is considered as well, then the capacitance of the sample exceeds that of the external capacitor. This is a second, although less stringent, requirement for a proper functionality of the ion probe.[77,78] Regardless, the bias voltage at the *a*-C:H surface cannot be measured directly and distortions of the applied pulse shape, therefore, cannot be completely excluded. The bias voltage as measured over the external capacitor is indicated in Fig. 8. The manually regulated frequency of the applied waveform signal is 1–12 kHz with a duty cycle of 90%.

The etch rate in Fig. 8 shows a nearly threefold increase when going from floating potential to a bias voltage of −9.1 V. This jump is repeated near the end of the measurement with a doubling of the etch rate. The etch rate in between both jumps steadily decreases together with the bias voltage. The effect of the surface roughness, which increased from about 5 to 26 nm, can however not be excluded as an alternative cause for this decreasing etch rate (Fig. 4). Nevertheless, both jumps in etch rate at the beginning and end of the measurement indicate that the ions in our hydrogen plasmas play a role in *a*-C:H etching even though they contribute less than 0.02% to the total incident flux.

TABLE II. The activation energy for different plasma systems, as determined from Figs. 8 and 9. The arc current is 60 A for all systems. The background pressure is 100 Pa, unless otherwise specified. The last column shows the temperature range for which the activation energy was fitted. BG indicates gas injection directly in the background of the reactor.

Plasma conditions	E_a (eV)	T^{-1} (10^{-3}K^{-1})
50 sccs H_2, 100 Pa	0.259 ± 0.003	1.73 – 2.54
50 sccs H_2, 25 Pa	0.284 ± 0.005	1.81 – 2.54
50 sccs H_2, 25 Pa	0.094 ± 0.005	2.54 – 2.86
50 sccs H_2, 25 Pa	1.1 ± 0.1	2.92 – 3.00
50 sccs Ar, 1 sccs H_2 (BG)	0.227 ± 0.002	1.95 – 2.58
50 sccs Ar, 1 sccs H_2 (arc)	0.265 ± 0.002	1.95 – 2.58
50 sccs Ar, 1 sccs D_2 (arc)	0.221 ± 0.003	1.95 – 2.58

C. Etch rates Ar/H_2 and Ar/D_2 plasmas

Fig. 9 shows the etch rate as function of the inverse substrate temperature for Ar/H_2 and Ar/D_2 plasmas. The etch rates are comparable for H_2 and D_2 when these gasses are injected via the arc, which is consistent with the small isotopic effect on the etch yields at low temperatures.[16,36] Direct injection of H_2 into the reactor systematically lowers the etch rate as can be seen in the graph. This indicates a more efficient hydrogen radical production in the arc than within the reactor. The etch yields themselves are on the order of 10^{-2}.

Previous work in our group by Gielen *et al.* returned an etch rate of 18 – 60 nm/min for soft and hard *a*-C:H films.[65] Based on these etch rates and the experimental conditions (100 sccs Ar, 10 sccs H_2, 48 A arc current) as used by Gielen *et al.*, the Ar^+ ion flux is expected to be lower than in our case. Gielen *et al.* furthermore reported an activation energy of about 0.43 eV ($1.7 - 1.9 \times 10^{-3}$ K^{-1}).[65] Activation energies for the three plasma systems in Fig. 9 are determined over the inverse temperature range from 1.73×10^{-3} up to

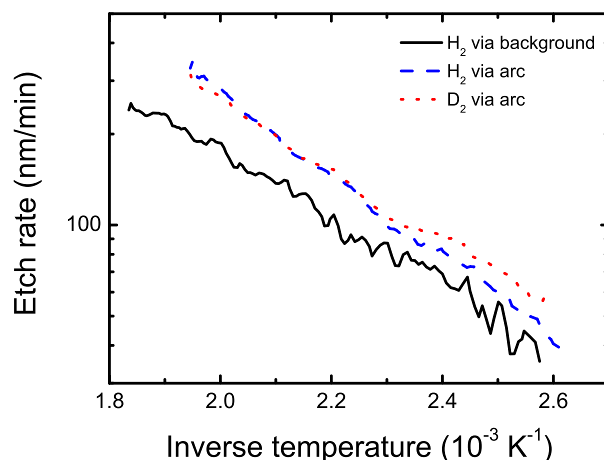

FIG. 9. The etch rate of *a*-C:H in an argon plasma (50 sccs, 60 A, 100 Pa), admixed with 1 sccs of H_2 injected via the background (full line), H_2 injected via the arc (dashed line), or D_2 injected via the arc (dotted line).

Downloaded 22 Jul 2012 to 130.209.6.40. Redistribution subject to AIP license or copyright; see http://jap.aip.org/about/rights_and_permissions

2.54×10^{-3} K^{-1}. The results—listed in the second part of Table II—vary from 0.221 ± 0.003 to 0.265 ± 0.002 eV and are much lower than Gielen's value. A variation in the sample properties, such as the density or sp^2 to sp^3 ratio, between ours and Gielen's work is a probable cause for this difference in activation energy.

The last result shown in this section concerns the roughness evolution during carbon erosion. In contrast with the pure H_2 plasma where a large increase is seen, the roughness in these three mixed systems fluctuates only about 1 nm around the initial value (Fig. 10). Larger variations are only observed near the end of the sample's lifetime, during which the last remnants of the carbon layer are removed. Furthermore, the minima and maxima in the surface roughness coincide for the Ar/H_2 and Ar/D_2 plasmas, but runs out of phase after $\sim$2 min for the Ar/H_2:BG plasma. This delay in the roughness evolution corresponds with the lower etch rate for the Ar/H_2:BG plasma, relative to the Ar/H_2 and Ar/D_2 plasmas. The roughness evolution for both pure and mixed plasma systems will be further discussed in Sec. VI.

VI. DISCUSSION

The discussion has been divided into two parts. Etch rates as well as ion and radical fluxes are compared for the pure hydrogen and mixed argon plasma systems in part one. A qualitative explanation for the etching mechanisms in these plasma systems are likewise formulated in this part, with the understanding that the processes and variables involved in plasma-surface interactions are—even if only due to the wide range in properties of amorphous carbon—numerous and intrinsically interconnected.[18,84–86] The roughness evolution during *a*-C:H etching is discussed in part two of this section.

A. Etch mechanism

The etch rate of *a*-C:H as well as the incident ion and radical flux in both Ar/H_2 and H_2 plasmas have been determined in the experimental results for a range of background pressures and substrate temperatures. These plasma systems are compared in Table III for a substrate temperature of 514 K and a 100 Pa background pressure. The etch rate in a pure argon plasma, which has not been discussed in Sec. V, is given as reference. Table III shows that the etch rate in an Ar/H_2 plasma exceeds the etch rate in both a pure H_2 and a pure Ar plasma by an order of magnitude. This also applies to the sum of the etch rates in these pure plasma systems. The ion flux is likewise 1–2 orders higher in an Ar/H_2 plasma compared to a pure H_2 plasma, whereas the atomic H flux decreases by a factor of 3 or more. Even so, the etch rate in an Ar plasma remains low despite the much higher Ar^+ ion flux and an absence of atomic H. These results indicate a synergistic effect between Ar^+ ions and atomic H in *a*-C:H etching. Atomic H, as was previously discussed in Sec. V B for a H_2 plasma, plays a dominant role in these expanding thermal plasmas. Section V B furthermore showed that hydrogen ions in a pure H_2 plasma do play a role in *a*-C:H etching, even though in our case they make up less than 0.02% of the total incident flux. To put this in perspective, the ion flux in an Ar/H_2 plasma is about 0.5% of the total flux. This allows for the possibility of a synergistic effect in a pure H_2 plasma as well.

Physical and chemical sputtering can immediately be ruled out as a possible etch mechanism due to the low ion energies involved in these plasmas. The ion energy distribution function at floating potential has a peak around 1 – 2 eV, whereas the C-C and C-H bonds have a binding energy of about 3 – 5 eV.[51,68] An alternative synergistic etch mechanism is ion-assisted chemical erosion. The yield of 10^{-2} determined in Sec. IV C for an Ar/H_2 plasma is in line with the yields (10^{-3} to 1) found in literature for ion-assisted chemical erosion, thereby considering the variety in ion energies and fluxes.[1,10,14,16,17,47,48] Ion-assisted chemical erosion—but also chemical erosion—in a pure H_2 plasma has however much higher yield values in literature than the 2×10^{-4} found in this work.[1,10,14,16,35,36,40,47,48] Lower yields, thus lower etch rates, can be attributed to changes in surface roughness, composition (i.e. sp^2 to sp^3 ratio) and surface coverage during etching. A decrease in etch rate, associated with an increasing surface roughness, has been established in Sec. V B. This will be further expanded upon in Sec. VI B.

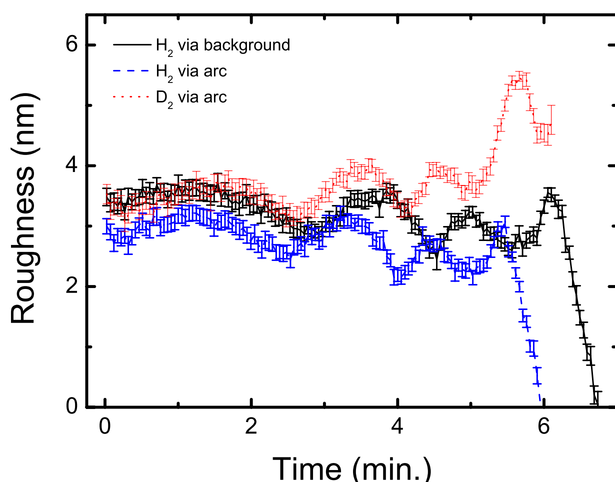

FIG. 10. The roughness of three different *a*-C:H samples exposed to an argon plasma (50 sccs, 60 A, 100 Pa), admixed with 1 sccs of (full line) H_2 injected via the background, (dashed line) H_2 injected via the arc, and (dotted line) D_2 injected via the arc. All three samples are completely eroded as indicated by the large variation in roughness that starts around 5 min.

TABLE III. The etch rate and flux for different plasma systems at a substrate temperature of 514 K. The arc current and background pressure are 60 A and 100 Pa, respectively, for all systems. BG indicates gas injection directly in the background of the reactor.

Plasma conditions	Etch rate (nm/min)	Ion flux (m^{-2} s^{-1})	Radical flux (m^{-2} s^{-1})
50 sccs Ar	$\sim$7	1.4×10^{22}	n/a
50 sccs Ar, 1 sccs H_2 (BG)	$\sim$198	1.1×10^{20}	2.3×10^{22}
50 sccs Ar, 1 sccs H_2 (arc)[a]	$\sim$335	8.5×10^{19}	
50 sccs H_2	$\sim$21	4.4×10^{18}	7.8×10^{22}

[a]H_2 injection through the arc, rather than directly in the reactor, is furthermore expected to yield a higher H flux in an Ar/H_2 plasma.

Downloaded 22 Jul 2012 to 130.209.6.40. Redistribution subject to AIP license or copyright; see http://jap.aip.org/about/rights_and_permissions

The activation energy of $\sim 0.2 - 0.3$ eV in both Ar/H_2 and H_2 plasmas is likewise lower than previously reported values for both chemical erosion ($1.6 - 2.5$ eV) and ion-assisted chemical erosion (~ 0.6 eV) of *a*-C:H or graphite.[27,33,35,36,41,45,46] As mentioned earlier in Sec. II, the energy gain due to relaxation of the carbon network during the erosion process leads to a reduced activation energy compared to the binding energy.[33] Differences in the initial configuration of the *a*-C:H-network, i.e., the sample characteristics in terms of the density or sp^2 to sp^3 ratio, can therefore affect the activation energy and etch rate. Changes in the surface roughness or sp^2 to sp^3 ratio during etching can likewise alter the binding network and, therefore, influence the activation energy.[15,87] In ion-assisted chemical erosion, the activation energy can be provided — in whole or partially — by the kinetic or recombination energy of the incident ion. It is thus likewise conceivable that the activation energy is affected by the composition of the incident ion flux (Ar^+ to H_3^+ ratio) in addition to the recombination energy and chemical reactivity of each ion species.

It is furthermore entirely possible that a significantly lower activation energy, as determined in this paper, indicates an alternative or secondary erosion mechanism. A large drop in etch rate can moreover be seen around 350 K in Fig. 7, which is expected to occur closer to 400 K if chemical erosion is the only etch mechanism involved. Swift chemical sputtering is a third etch mechanism known to occur for very low ion energies which could explain the observed erosion below 400 K.[52,55,56] SCS has, however, no inherent temperature dependent etch rate and has only been observed in numerical modelling for very high H fluxes (up to 10^{29} m^{-2} s^{-1}).[52] Whether SCS partakes in these low energetic, high flux hydrogen plasmas is a dispute that requires further microscopic investigation and numerical modelling. Though, such an investigation falls outside the scope of this paper. The influence, if any, of the ion flux composition on the activation energy can likewise be a point of interest for future experimental work.

B. Surface roughness

Intense ion bombardment of *a*-C:H in deposition studies has shown a decreasing surface roughness with increasing ion energy up to around 50 eV, after which the surface roughness remained smooth (<2 nm) up to 10 keV.[88–91] Thermal spikes at the surface caused by the recombination energy of low energetic ions with an electron promote the surface mobility of existing sp^2 groups and graphitization of the material.[92–94] Suppression of the sp^3 bonding by these low energy Ar^+ and C^+ ions is associated with a rough surface.[89,90] An increased substrate temperature (>450 K) likewise promotes surface mobility and thus surface roughness.[88,89,93,95] A higher sp^2 fraction and more interconnected carbon furthermore leads to lower etch rates, even though atomic H preferentially attack sp^2 over sp^3 sites.[27,93] The (initial) sp^2 content of the material is therefore an important factor in whether additional atomic H etching during (or after) deposition results in either an increase or decrease of the surface roughness. Regardless thereof, the reported surface roughness after deposition (or post-deposition treatment) is on the order of nanometers.[37,91,93,96]

A surface roughness of a few nanometers is of the same order as the roughness found in this work during Ar/H_2 (or Ar/D_2) plasma etching. The roughness in a pure H_2 plasma on the other hand increased strongly as established in Sec. V B. The etch rate, moreover, decreased once a larger surface roughness was developed. These are surprising results since higher surface exposure and H trapping within the roughness layer should increase the etch rate as well as the roughness roughness.[83,97] The following additional effects have to be taken into account to understand both the etch rate and the roughness.

First, H saturation of the *a*-C:H surface in a high flux regime decreases the carbon collision cross section.[38,51,52,98] H shielding, therefore, lowers the etch rate.

Second, graphite is known to have a high surface-recombination probability (up to 80%) for atomic H in the energy regime ($0.05 - 0.9$ eV) of our etch plasmas.[99,100] Since molecular hydrogen does not etch carbon,[101] a similarly high recombination probability for *a*-C:H would likewise contribute to a decrease in the etch rate. A high surface roughness, moreover, implies that hydrogen conversion occurs preferentially within the trenches and valleys of the roughness layer. This should however lead to a flattening of the surface roughness or at the very least place a limit on the size of the surface roughness. This effect is a possible explanation for the observed roughness fluctuation of about 1 nm during Ar/H_2 etching, but not for the extreme surface roughness measured during pure H_2 etching.

Third, the etch rate is affected by changes in the material composition. As stated earlier, graphitic (i.e., sp^2 rich) has a lower etch rate than diamond-like (i.e., sp^2 poor) amorphous carbon.[27] Local variations in the sp^2 content as well as the formation of graphitic clusters lead to a roughness development.[92,93] These graphitic clusters act as a capping layer, similar to *a*-Si patches in *c*-Si etching (Fig. 11).[83] The incident ions promote graphitization via thermal spikes due to ion recombination with an electron, but likewise enhance the

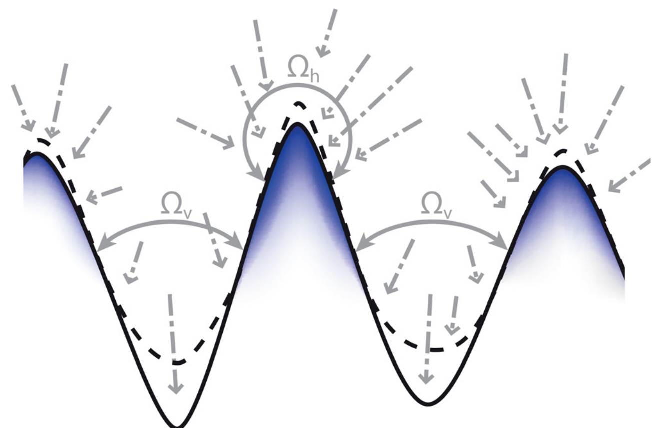

FIG. 11. The incident ion flux is larger at the hills than in the valleys due to a larger opening angle Ω_h and a low reflection coefficient. Thermal spikes caused by these ions promote the formation of graphitic clusters, which then act as a capping layer. This leads to a high surface roughness. Dashed line is the original roughness; full line is after etching.

Downloaded 22 Jul 2012 to 130.209.6.40. Redistribution subject to AIP license or copyright; see http://jap.aip.org/about/rights_and_permissions

erosion rate as evident from the synergistic effect in the Ar/H_2 plasmas. The two extremes, as an illustration, are purely graphitization by the low amount of ions in a H_2 plasma and purely an enhanced etch rate by the high ion flux in Ar/H_2 plasmas. A low ion flux incident to the hills and upper parts of the sidewalls of the roughness layer will consequently roughen the layer, as visualized in Fig. 11, whereas a large ion flux will smoothen it. The opening angle — through which ions or radicals can reach the surface — is larger on the hill tops than within the valleys, thereby creating an imbalance in the flux between hills and valleys (Fig. 11). H^+ ions have furthermore a reflection coefficient below 0.2 around 1 eV, with a maximum of $\sim$0.6 around 5 eV.[39] The atomic H reflection is expected to be higher, up to 0.8 depending on the kinetic energy and angle of incidence.[51,102,103] More radicals than ions, percentage wise, will thus reach the valleys. This strengthens the view that ions primarily affect the hills and upper parts of the sidewalls of the roughness layer. The mechanism described in this last point explains the roughness evolution observed for both H_2 and Ar/H_2 plasmas.

VII. SUMMARY

Hydrogenated amorphous carbon thin films were successfully etched with both ions and neutrals far below the threshold of physical sputtering and even below the required energy to break C-C and C-H bonds ($\sim 3 - 5$ eV). Moreover, the experimental results indicated a synergistic effect in the etch rate for Ar/H_2 and Ar/D_2 plasmas. Ion-assisted chemical sputtering is the primary etch mechanism in these low-energetic high flux plasmas. Lower etch yields in pure H_2 plasmas are attributed to H shielding of the *a*-C:H surface. The etch rate at low substrate temperatures furthermore suggests a contribution of swift chemical sputtering. Further studies (on the microscopic level) are however required to resolve this issue. Last, thermal spikes at the surface caused by the recombination energy of incident ions with electrons lead to graphitization and determine to a large extent the surface morphology during plasma etching.

ACKNOWLEDGMENTS

We would like to thank W. Keuning for the SEM measurements and V. Vandalon for the AFM measurements. We also greatly appreciate the skillful technical assistance of M. J. F. van de Sande, J. J. L. M. Meulendijks, H. M. M. de Jong, and J. J. A. Zeebregts. This work is part of the research program of the Dutch Foundation for Fundamental Research on Matter (FOM-TFF). It is also supported by the European Communities under the contract of Association between EURATOM and FOM and carried out within the framework of the European Fusion Programme.

[1] J. Roth, J. Nucl. Mater. **266–269**, 51 (1999).
[2] A. Kukushkin, H. Pacher, G. Pacher, G. Janeschitz, D. Coster, A. Loarte, and D. Reiter, Nucl. Fusion **43**, 716 (2003).
[3] A. W. Kleyn, W. Koppers, and N. Lopes Cardozo, Vacuum **80**, 1098 (2006).
[4] P. Wienhold, V. Philipps, A. Kirschner, A. Huber, J. von Seggern, H. G. Esser, D. Hildebrandt, M. Mayer, M. Rubel, and W. Schneider, J. Nucl. Mater. **313**, 311 (2003).
[5] J. Roth, E. Tsitrone, and A. Loarte, Nucl. Instrum. Methods Phys. Res. B **258**, 253 (2007).
[6] C. H. Skinner and G. Federici, Phys. Scr. T **124**, 18 (2006).
[7] N. Holtkamp, Fusion Eng. Des. **84**, 98 (2009); Proceeding of the 25th Symposium on Fusion Technology — (SOFT-25).
[8] N. Yu. Svechnikov, V. G. Stankevich, A. M. Lebedev, K. A. Menshikov, B. N. Kolbasov, M. I. Guseva, K. Y. Vukolov, D. Rajarathnam, N. M. Kocherginsky, and Yu. Kostetski, Fusion Eng. Des. **75–79**, 339 (2005).
[9] A. Litnovsky, V. Voitsenya, T. Sugie, G. De Temmerman, A. E. Costley, A. J. H. Donne, K. Yu. Vukolov, I. Orlovskiy, J. N. Brooks, J. P. Allain *et al.*, Nucl. Fusion **49**, 075014 (2009).
[10] J. Roth, Phys. Scr. T **124**, 37 (2006).
[11] V. Philipps, E. Vietzke, M. Erdweg, and K. Flaskamp, J. Nucl. Mater. **145–147**, 292 (1987).
[12] J. Biener, U. A. Schubert, A. Schenk, B. Winter, C. Lutterloh, and J. Küppers, J. Chem. Phys. **99**, 3125 (1993).
[13] A. Annen and W. Jacob, Appl. Phys. Lett. **71**, 1326 (1997).
[14] B. V. Mech, A. A. Haasz, and J. W. Davis, J. Nucl. Mater. **255**, 153 (1998).
[15] B. Landkammer, A. von Keudell, and W. Jacob, J. Nucl. Mater. **264**, 48 (1999).
[16] M. Balden and J. Roth, J. Nucl. Mater. **280**, 39 (2000).
[17] C. Hopf, A. von Keudell, and W. Jacob, Nucl. Fusion **42**, L27 (2002).
[18] M. Schlüter, C. Hopf, T. Schwarz-Selinger, and W. Jacob, J. Nucl. Mater. **376**, 33 (2008).
[19] H. F. Winters and J. W. Coburn, Surf. Sci. Rep. **14**, 161 (1992).
[20] J. W. A. M. Gielen, M. C. M. van de Sanden, P. R. M. Kleuskens, and D. C. Schram, Plasma Sources Sci. Technol. **5**, 492 (1996).
[21] J. Benedikt, R. V. Woen, S. L. M. van Mensfoort, V. Perina, J. Hong, and M. C. M. van de Sanden, Diamond Rel. Mater. **12**, 90 (2003); Proceedings of the 4th Specialist Meeting on Amorphous Carbon.
[22] J. W. Weber, T. A. R. Hansen, M. C. M. van de Sanden, and R. Engeln, J. Appl. Phys. **106**, 123503 (2009).
[23] D. Larson, L. Lott, and D. Cash, Appl. Opt. **12**, 1271 (1973).
[24] V. Paret, A. Sadki, Y. Bounouh, R. Alameh, C. Naud, M. Zarrabian, A. Seignac, G. Turban, and M. L. Thèye, J. Non-Cryst. Solids **227–230**, 583 (1998).
[25] P. Lemoine, J. P. Quinn, P. D. Maguire, and J. A. D. McLaughlin, Carbon **44**, 2617 (2006).
[26] H. Fujiwara, *Spectroscopic Ellipsometry: Principles and Applications* (John Wiley & Sons, Chichester, UK, 2007).
[27] A. von Keudell and W. Jacob, J. Appl. Phys. **79**, 1092 (1996).
[28] C. Hopf, A. von Keudell, and W. Jacob, J. Appl. Phys. **93**, 3352 (2003).
[29] N. Maitre, S. Camelio, A. Barranco, Th. Girardeau, and E. Breelle, J. Non-Cryst. Solids **351**, 877 (2005).
[30] G. S. Oehrlein, T. Schwarz-Selinger, K. Schmid, M. Schlüter, and W. Jacob, J. Appl. Phys. **108**, 043307 (2010).
[31] G. E. Jellison and F. A. Modine, Appl. Phys. Lett. **69**, 371 (1996).
[32] B. Johs and J. S. Hale, Phys. Status Solidi A **205**, 715 (2008).
[33] W. Jacob, Thin Solid Films **326**, 1 (1998).
[34] W. Jacob and J. Roth, "Chemical Sputtering," in *Sputtering by Particle Bombardment* (Springer, Berlin, 2007), Vol. 110.
[35] A. Horn, A. Schenk, J. Biener, B. Winter, C. Lutterloh, M. Wittmann, and J. Küppers, Chem. Phys. Lett. **231**, 193 (1994).
[36] J. Biener, A. Schenk, B. Winter, C. Lutterloh, A. Horn, and J. Küpper, Vacuum **46**, 903 (1995).
[37] B. N. Jariwala, C. V. Ciobanu, and S. Agarwal, J. Appl. Phys. **106**, 073305 (2009).
[38] C. Lutterloh, A. Schenk, J. Biener, B. Winter, and J. Küppers, Surf. Sci. **316**, L1039 (1994).
[39] E. Vietzke, Contrib. Plasma Phys. **42**, 590 (2002).
[40] E. Vietzke, K. Flaskamp, V. Philipps, G. Esser, P. Wienhold, and J. Winter, J. Nucl. Mater. **145–147**, 443 (1987).
[41] J. Biener, A. Schenk, B. Winter, C. Lutterloh, U. A. Schubert, and J. Küppers, Surf. Sci. **307–309**(1), 228 (1994).
[42] K. Ashida, K. Ichimura, M. Matsuyama, and K. Watanabe, J. Nucl. Mater. **128–129**, 792 (1984).
[43] S. Fukuda, T. Hino, and T. Yamashina, J. Nucl. Mater. **162–164**, 997 (1989).
[44] T. Kugimiya, M. Kannaka, M. Yokomizo, A. Nakaue, and H. Takamatsu, J. Electrochem. Soc. **153**, C282 (2006).
[45] E. Vietzke, K. Flaskamp, and V. Philipps, J. Nucl. Mater. **111–112**, 763 (1982).
[46] A. von Keudell and W. Möller, J. Appl. Phys. **75**, 7718 (1994).

Downloaded 22 Jul 2012 to 130.209.6.40. Redistribution subject to AIP license or copyright; see http://jap.aip.org/about/rights_and_permissions

[47]J. Roth, R. Preuss, W. Bohmeyer, S. Brezinsek, A. Cambe, E. Casarotto, R. Doerner, E. Gauthier, G. Federici, S. Higashijima *et al.*, Nucl. Fusion **44**, L21 (2004).
[48]P. Starke, U. Fantz, and M. Balden, J. Nucl. Mater. **337**, 1005 (2005).
[49]R. Yamada, K. Nakamura, K. Sone, and M. Saidoh, J. Nucl. Mater. **95**, 278 (1980).
[50]C. Hopf, A. von Keudell, and W. Jacob, J. Appl. Phys. **94**, 2373 (2003).
[51]C. O. Reinhold, P. S. Krstic, and S. J. Stuart, Nucl. Instrum. Methods Phys. Res. B **267**, 691 (2009).
[52]E. Salonen, K. Nordlund, J. Keinonen, and C. H. Wu, Phys. Rev. B **63**, 195415 (2001).
[53]A. V. Krasheninnikov, K. Nordlund, E. Salonen, J. Keinonen, and C. H. Wu, Comp. Mater. Sci. **25**, 427 (2002).
[54]E. Salonen, Phys. Scr. T **111**, 133 (2004).
[55]K. Nordlund, E. Salonen, A. Krasheninnikov, and J. Keinonen, Pure Appl. Chem. **78**, 1203 (2006).
[56]K. Nordlund, E. Salonen, J. Keinonen, and C. H. Wu, Nucl. Instrum. Methods Phys. Res. B **180**, 77 (2001).
[57]V. Philipps, E. Vietzke, and H. Trinkaus, J. Nucl. Mater. **179–181**, 25 (1991).
[58]P. N. Maya, U. von Toussaint, and C. Hopf, New J. Phys. **10**, 023002 (2008).
[59]J. Robertson, Mater. Sci. Eng. R. **37**, 129 (2002).
[60]S. Logothetidis, Diamond Relat. Mater. **12**, 141 (2003).
[61]E. Salançon, T. Dürbeck, T. Schwarz-Selinger, and W. Jacob, J. Nucl. Mater. **363–365**, 944 (2007).
[62]J. W. A. M. Gielen, P. R. M. Kleuskens, M. C. M. van de Sanden, L. J. van Ijzendoorn, D. C. Schram, E. H. A. Dekempeneer, and J. Meneve, J. Appl. Phys. **80**, 5986 (1996).
[63]J. W. Weber, Master's thesis, Eindhoven University of Technology, Eindhoven, 2009.
[64]D. E. Aspnes, Thin Solid Films **89**, 249 (1982).
[65]J. W. A. M. Gielen, W. M. M. Kessels, M. C. M. van de Sanden, and D. C. Schram, J. Appl. Phys. **82**, 2643 (1997).
[66]S. S. Zumdahl, *Chemical Principles*, 3rd ed. (Houghton Mifflin, Boston, MA, 1998).
[67]M. C. M. van de Sanden, G. M. Janssen, J. M. de Regt, D. C. Schram, J. A. M. van der Mullen, and B. van der Sijde, Rev. Sci. Instrum. **63**, 3369 (1992).
[68]P. Kudlacek, R. F. Rumphorst, and M. C. M. van de Sanden, J. Appl. Phys. **106**, 073303 (2009).
[69]M. C. M. van de Sanden, J. M. de Regt, and D. C. Schram, Phys. Rev. E **47**, 2792 (1993).
[70]M. J. de Graaf, R. Severens, R. P. Dahiya, M. C. M. van de Sanden, and D. C. Schram, Phys. Rev. E **48**, 2098 (1993).
[71]P. Vankan, D. C. Schram, and R. Engeln, Chem. Phys. Lett. **400**, 196 (2004).
[72]D. K. Otorbaev, A. J. M. Buuron, N. T. Guerrassimov, M. C. M. van de Sanden, and D. C. Schram, J. Appl. Phys. **76**, 4499 (1994).
[73]R. F. G. Meulenbroeks, A. J. van Beek, A. J. G. van Helvoort, M. C. M. van de Sanden, and D. C. Schram, Phys. Rev. E **49**, 4397 (1994).
[74]R. F. G. Meulenbroeks, R. A. H. Engeln, M. N. A. Beurskens, R. M. J. Paffen, M. C. M. van de Sanden, J. A. M. van der Mullen, and D. C. Schram, Plasma Sources Sci. Technol. **4**, 74 (1995).
[75]W. M. M. Kessels, C. M. Leewis, M. C. M. van de Sanden, and D. C. Schram, J. Appl. Phys. **86**, 4029 (1999).
[76]G. M. W. Kroesen, D. C. Schram, and J. C. M. de Haas, Plasma Chem. Plasma Process. **10**, 531 (1990).
[77]N. S. J. Braithwaite, J. P. Booth, and G. Cunge, Plasma Sources Sci. Technol. **5**, 677 (1996).
[78]M. C. Petcu, A. C. Bronneberg, A. Sarkar, M. A. Blauw, M. Creatore, and M. C. M. van de Sanden, Rev. Sci. Instrum. **79**, 115104 (2008).
[79]M. A. Lieberman and A. J. Lichtenberg, *Principles of Plasma Discharges and Materials Processing*, 2nd ed. (John Wiley & Sons, Hoboken, New Jersey, 2005).
[80]S. Mazouffre, P. Vankan, R. Engeln, and D. C. Schram, Phys. Plasmas **8**, 3824 (2001).
[81]M. C. M. van de Sanden and J. A. Tobin, Plasma Sources Sci. Technol. **7**, 28 (1998).
[82]E. Langereis, S. B. S. Heil, H. C. M. Knoops, W. Keuning, M. C. M. van de Sanden, and W. M. M. Kessels, J. Phys. D: Appl. Phys. **42**, 073001 (2009).
[83]A. A. E. Stevens and H. C. W. Beijerinck, J. Vac. Sci. Technol. A **23**, 126 (2005).
[84]W. Möller, Appl. Phys. A **56**, 527 (1993).
[85]A. von Keudell, Plasma Sources Sci. Technol. **9**, 455 (2000).
[86]M. Cacciatore and M. Rutigliano, Phys. Scr. **78**, 058115 (2008).
[87]R. Petri, P. Brault, O. Vatel, D. Henry, E. André, P. Dumas, and F. Salvan, J. Appl. Phys. **75**, 7498 (1994).
[88]Y. Lifshitz, G. D. Lempert, and E. Grossman, Phys. Rev. Lett. **72**, 2753 (1994).
[89]Y. Lifshitz, Diamond Relat. Mater. **5**, 388 (1996).
[90]E. Grossman, G. D. Lempert, J. Kulik, D. Marton, J. W. Rabalais, and Y. Lifshitz, Appl. Phys. Lett. **68**, 1214 (1996).
[91]G. Capote, R. Prioli, and F. L. Freire, Jr., J. Vac. Sci. Technol. A **24**, 2212 (2006).
[92]M. Chhowalla, A. C. Ferrari, J. Robertson, and G. A. J. Amaratunga, Appl. Phys. Lett. **76**, 1419 (2000).
[93]X. L. Peng, Z. H. Barber, and T. W. Clyne, Surf. Coat. Technol. **138**, 23 (2001).
[94]C. Casiraghi, A. C. Ferrari, R. Ohr, A. J. Flewitt, D. P. Chu, and J. Robertson, Phys. Rev. Lett. **91**, 226104 (2003).
[95]M. Pandey, D. Bhatacharyya, D. S. Patil, K. Ramachandran, and N. Venkatramani, Surf. Coat. Technol. **182**, 24 (2004).
[96]K. H. Lai, C. Y. Chan, M. K. Fung, I. Bello, C. S. Lee, and S. T. Lee, Diamond Relat. Mater. **10**, 1862 (2001).
[97]Y. Zhao, J. Drotar, G. Wang, and T. Lu, Phys. Rev. Lett. **82**, 4882 (1999).
[98]E. Salonen, K. Nordlund, J. Tarus, T. Ahlgren, J. Keinonen, and C. H. Wu, Phys. Rev. B **60**, R14005 (1999).
[99]M. Cacciatore and M. Rutigliano, Phys. Scr. T **124**, 80 (2006).
[100]M. Rutigliano and M. Cacciatore, ChemPhysChem **9**, 171 (2008).
[101]T. Yoshitake, T. Nishiyama, and K. Nagayama, Diamond Relat. Mater. **9**, 689 (2000).
[102]M. Mayer, W. Eckstein, and B. M. U. Scherzer, J. Appl. Phys. **77**, 6609 (1995).
[103]E. Vietzke, M. Wada, and M. Hennes, J. Nucl. Mater. **266–269**, 324 (1999).

Downloaded 22 Jul 2012 to 130.209.6.40. Redistribution subject to AIP license or copyright; see http://jap.aip.org/about/rights_and_permissions